Article

Ice-Templating of Lignin and Cellulose Nanofiber-Based Carbon Aerogels: Implications for Energy Storage Applications

Bony Thomas, Shiyu Geng, Jiayuan Wei, Henrik Lycksam, Mohini Sain, and Kristiina Oksman*

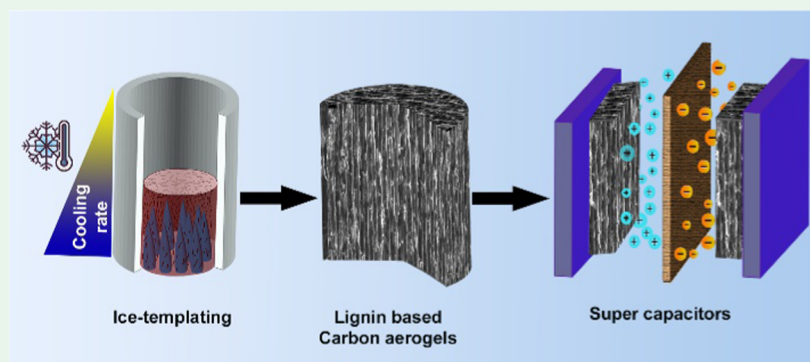Cite This: *ACS Appl. Nano Mater.* 2022, 5, 7954–7966

Read Online

| ACCESS | Metrics & More | Article Recommendations | Supporting Information |

Ice-templating → Lignin based Carbon aerogels → Super capacitors

ABSTRACT: Hierarchically porous carbon aerogels (CAs) were synthesized by following a green, facile preparation route involving ice-templating and lyophilization followed by carbonization. For the first time, we report CAs prepared with a cooling rate of 7.5 K/min, demonstrating a very high specific surface area (SSA) of 1260 $m^2\ g^{-1}$ without any physical or chemical activation steps, and the electrode prepared using the latter aerogel showed superior electrochemical performance with a specific capacitance of 410 F g^{-1} at 2 m V s^{-1} with a cyclic stability of 94% after 4500 charge–discharge cycles. The effects of the ice-templating cooling rate and the solid content of lignin and cellulose nanofibers (CNFs) in the suspension on the structure and electrochemical performance of the CAs were investigated. The ice-templating process and the cooling rate were found to have a large effect on the generation of the nanoporous structure and the specific surface area of carbon aerogels, while the solid content of the lignin-nanocellulose suspension showed negligible effects. When assembled as a supercapacitor (SC), a remarkable specific capacitance of 240 F g^{-1} at 0.1 A g^{-1} was achieved. The relaxation time constant for the prepared SC was 1.3 s, which shows the fast response of these SCs. In addition, an energy density of 4.3 Wh kg^{-1} was also obtained at a power density of 500 W kg^{-1}. Thus, this study opens new perspectives for the preparation of green, environment-friendly, free-standing, high-performance CA electrodes for future energy storage applications.

KEYWORDS: *carbon aerogels, ice-templating, nanoporous structure, supercapacitors, specific capacitance*

INTRODUCTION

Carbon aerogels (CAs) are materials having a three-dimensional (3D) hierarchical network structure with interconnected macro-, meso-, and micropores. Typically, CAs have a low density, high specific surface area (SSA), controllable pore size, and good chemical as well as mechanical stability, which have attracted increased research attention in recent years.[1−3] Different methods have been reported for the preparation of CAs such as pyrolysis of the organic polymer frameworks prepared using the sol−gel polymerization technique[4,5] and silica template-assisted techniques.[6] These techniques, however, had limitations; for example, the processes did not adequately address the issue of ion mobility due to a lack of adequate amount of mesoporous structures in the obtained CAs to facilitate the ion diffusion. Moreover, micropores obtained were smaller in sizes or were narrow in shape, resulting in poor accessibility for electrolyte ions, high cost, and complex preparation processes including physical or

chemical activation steps for generating high SSA.[7,8] With the increasing energy demand of the world, the need for an economical, renewable, and abundant alternative to the conventional carbon precursors has been explored by several researchers around the world using biomass. Among those, lignin-based CAs showed potential for future energy storage applications.[2,8]

One of the recent advancements for efficiently isolating lignin from black liquor is the invention of the LignoBoost process, which offers lignin with high purity, high yield, and
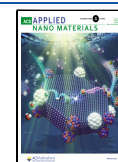
low ash and carbohydrate contents, with low investment and operation costs.[9,10] The high aromatic content in lignin, which results in a high carbon yield, is the key factor that makes lignin an attractive raw material for the preparation of CAs.[8,11,12] Due to their unique hierarchical pore structure with numerous interconnected pores in all ranges, i.e., micropores (<2 nm), mesopores (2−50 nm), and macropores (>50 nm), these CAs exhibit good electrical double-layer capacitance (EDLC). Yet their successful applications in energy storage devices demand even higher capacitance values of these electrodes to compete with the conventional carbon electrodes made using graphene or carbon nanotube.[8,11] Recently, an approach via ice-templating process followed by lyophilization and carbonization has emerged as a promising preparation route to manufacture lignin-based anisotropic porous carbons, which are useful for various applications like supercapacitors,[2,8,11,13] electromagnetic interference shielding (EMI) materials,[14,15] and for CO_2 capture.[11,16] Ice-templating is a segregation-induced templating process of a second phase (such as polymers, ceramics, or metals) using a solvent in which the second phase is either soluble or dispersible to facilitate crystal growth in their solidified phase. These solvent crystals are removed by sublimation, resulting in a templated porous structure where the pores replicate the morphology of solvent crystals.[17−19] There are several factors that influence the microstructure of ice-templated materials. The structure of the aerogels is strongly influenced by the freezing source and conditions. The freezing step can be done in different ways, for example, freezing the sample in a normal freezer (typically around −25 °C), which is enough for freezing aqueous suspensions, or using a liquid nitrogen bath (−196 °C) with a controlled cooling rate.[17,18] The nucleation mechanism of the ice crystals with respect to the source temperature has been well established. Ice crystal nucleation and growth are controlled by the degree of supercooling. If the supercooling is low, which is the case for normal freezer conditions, crystal growth is kinetically more favored than nucleation. Hence, the structure would consist of fewer numbers of larger pores after the sublimation process. However, in the case of a high degree of supercooling, as in the case of direct freezing in liquid nitrogen, nucleation is more dominant than crystal growth, resulting in a larger number of smaller pores.[18,19] It has been established that adjustments in the cooling rate and temperature gradient provide high control over the final pore size and pore orientation of the ice-templated structures.[17,19−21] The final morphology of the materials can also be tuned by changing the solid content of the suspension since the pore generation depends on the amount of water present in the suspension. It has been observed that a too low solid content in the initial suspension led to weaker structures, while a too high concentration resulted in nonporous microstructures.[18,20] In previous studies[11] on lignin-based CAs prepared through ice-templating, we reported that CAs consisting of kraft lignin and 2,2,6,6-tetramethylpiperidine-1-oxyl radical (TEMPO)-mediated oxidized cellulose nanofibers (CNFs), which were ice-templated from the suspension with a solid content of 6 wt % with a cooling rate of 10 K/min followed by lyophilization and carbonization, led to a specific capacitance of 129 F g^{-1} at a current density of 0.2 A g^{-1}.[11] In a comparative study performed by Thomas et al.,[8] CAs were prepared from different types of lignins and mechanically fibrillated CNFs, where the solid content of the initial suspension was 2.3 wt % and the ice-templating cooling rate was 10 K/min, showing a

higher specific capacitance of 163 F g^{-1}.[8] Even though these studies used the ice-templating technique for preparation of the lignin-/CNF-based CAs, the crucial importance of different ice-templating process parameters (solid content of the lignin/CNF suspensions and ice-templating cooling rates) on the final morphology, SSA, and electrochemical performances of CAs remains to be explored. Tuning the hierarchical pore structure of CAs by careful selection of ice-templating processing parameters can be beneficial for obtaining excellent electrodes for supercapacitors (SCs).

The aim of the current study was to investigate the importance of ice-templating process kinetics, such as the cooling rate (5, 7.5, and 10 K/min) as well as fiber−polymer interactions in lignin/CNF suspensions (3, 5, and 7 wt %) on the pore structure, and electrochemical performances of CAs. The hypothesis was that the hierarchical pore structure, ranging from micropores (<2 nm) to mesopores (2−50 nm) and macropores (>50 nm), can be tailored by the material composition and ice-templating parameter used. The results showed remarkable differences in the CA microstructure, porosity, specific surface area, and hence electrochemical performances because of the ice-templating process. The presented simple and green approach for the preparation of CAs has great potential for energy storage applications.

■ EXPERIMENTAL SECTION

Materials. BiochoiceTM lignin (L), based on softwood, was kindly supplied by Domtar Plymouth pulp mill (Plymouth, NC). Sodium hydroxide (NaOH) and acetic acid (CH$_3$COOH, 96%) were purchased from Merck KGaA (Darmstadt, Germany). High-purity sodium chlorite (NaClO$_2$, 77.5−82.5% chlorite content) and sulfuric acid (H$_2$SO$_4$, 95−98%) were purchased from VWR International AB (Stockholm, Sweden). CNFs used in this study were prepared according to the previous method reported by Berglund et al.[22] Briefly, carrot residue was alkali-washed for removing the hemicellulose and lignin contents, followed by bleaching using NaClO$_2$ to obtain a white pulp. After neutralization, the bleached pulp was subjected to ultrafine grinding in a super mass collider MKCA6-3, Masuko Sangyo Co (Kawaguchi-city, Japan), resulting in CNFs with 2 wt % solid content.

Preparation of Carbon Aerogels. As the first step in the preparation procedure for CAs, lignin (L) was dissolved in water by adding NaOH using a magnetic stirrer for 1 h at room temperature. Then, the suspension (2 wt %) was added into the dissolved L solution in required amounts to prepare L/CNF suspensions with different final solid contents (3, 5, 7 wt %), as shown in Table 1,

Table 1. Sample Coding, Cooling Rate (C), and Solid Content (W) of L/CNF Suspensions

sample coding (K/min)	ice-templating cooling rate	solid content (wt %)
C10W3	10	3
C10W5	10	5
C10W7	10	7
C7.5W7	7.5	7
C5W7	5	7

keeping the ratio of L to CNF as 75/25 in all suspensions. It was shown in a previous study that the higher ratio of lignin to CNF is important for a hierarchical porous structure.[8] The specific surface area increased from 436 to 750 m^{2}g^{-1} when the lignin content was increased from 60% to 80% in kraft lignin-based carbon aerogels. However, the SSA reduced drastically to 331 m^{2}g^{-1} when the lignin content increased to 88%. Hence, a ratio that is more prone to giving high SSA while keeping the idea of having enough CNF to act as the sacrificial template was chosen for this study.[8] These suspensions were
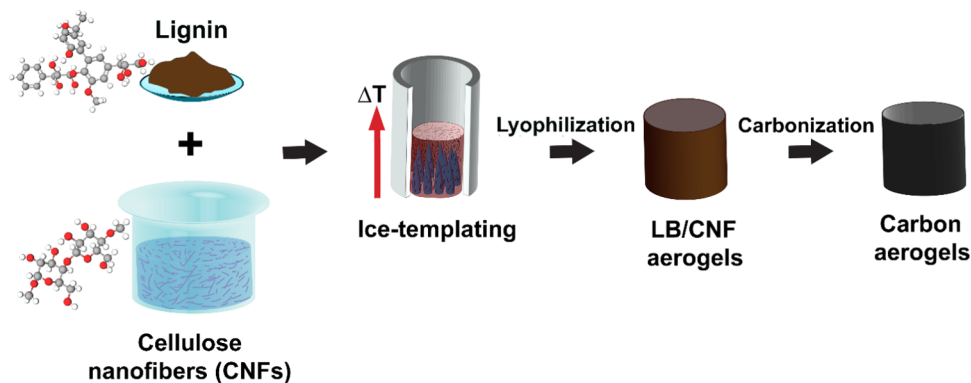
Figure 1. Schematic representation of various processes involved in the preparation of CAs.

stirred using a magnetic stirrer for 24 h at room temperature for achieving uniform distribution of the CNFs in the L and placed in the refrigerator overnight at 4 °C. Before proceeding to the ice-templating process, all of the suspensions were mixed in a high-speed rapid mixer (SpeedMixer DAC 150.1, High Wycombe, U.K.) at 2000 rpm for 2 min.

The ice-templating process was done by pouring the L/CNF suspensions into a Teflon mold, which was fixed on the top of a copper rod. The bottom end of the copper rod was dipped into a liquid nitrogen bath (at −196 °C), and the cooling rates during ice-templating were controlled (10, 7.5, and 5 K/min) using a temperature controller connected at the top of the copper rod. Major processing steps of the CAs are schematically represented in Figure 1. Using higher-solid-content L/CNF suspensions (7 wt %) for varying the ice-templating cooling rate would be advantageous for creating more nucleation sites and hence smaller macropores compared to those CAs made from lower-solid-content L/CNF suspensions (3 and 5 wt %). This will increase the retention time for electrolyte ions during discharging of the supercapacitor. However, increasing the solid content above 7 wt % would result in highly viscous L/CNF suspensions, limiting the possibility of performing a bubble-free ice-templating process, which is a critical step in the preparation of carbon aerogels.

Due to the temperature difference between top and bottom ends of the suspension in the Teflon mold, unidirectional freezing is achieved. After freezing was completed, the ice-templated material was transferred to a freezer at −20 °C and kept for minimum 3 h before the lyophilization process. Martin Christ α 1-2 LD plus lyophilizer (LABEX Instrument AB, Helsingborg, Sweden) was employed at 1 mbar pressure, for 72 hours, at a shelf temperature of 30 °C for converting the frozen samples into L/CNF aerogels. For carbonizing the L/CNF aerogels to CAs, the Nabertherm RHTC-230/15 horizontal tube furnace in a N_2 atmosphere (ATHAM AB, Hässelby, Sweden) was used. As reported in our previous study, the carbonization procedure was chosen to obtain a high carbon content, high SSA, electrode wettability, and an interconnected and hierarchical porous structure for the CAs.[8] L/CNF aerogels were initially heated from room temperature to 100 °C and kept isothermally at 100 °C for 1 h to remove the entrapped moisture from aerogels. To maximize the release of the volatiles and stabilize the L/CNF aerogels for further heat treatment, L/CNF aerogels were heated to 400 °C followed by isothermal holding at 400 °C for 1 h. Later, the temperature was increased from 400 to 1000 °C and maintained at 1000 °C for 1 h to complete the carbonization procedure.[8] Lower carbonization temperatures would lead to predominantly amorphous carbon with a relatively lower SSA and hence conductivities, while higher carbonization temperatures would result in ordered, partially graphitic and hydrophobic carbon, which is not wettable by the electrolyte.[6,8,11] Therefore, the carbonization temperature was kept at 1000 °C, which was found to be suitable for preparing stable carbon aerogels with good electrochemical performances.[8,11] All of the heating steps in the process were done at a fixed heating rate of 5 °C/min. After cooling to room temperature, CAs

were taken out from the furnace and washed three times with 0.1 M acetic acid for a duration of 1 h for each washing. Afterward, these CAs were washed with distilled water to remove the traces of acetic acid, until the pH of the water became neutral. Properly washed CAs were transferred carefully to a vacuum oven and dried at 80 °C overnight to obtain the final CAs for further characterization.

Characterization. Cellulose nanofibers (CNFs) were analyzed for their topographic information using atomic force microscopy (AFM) under the tapping mode with a Veeco MultiMode scanning probe (Santa Barbara) and Bruker TESPA tips (Camarillo). Very dilute suspensions of CNFs (.001 wt %) were drop-casted onto a freshly cleaved mica sheet and dried in the vacuum oven at 80 °C. AFM height images were captured for determining the width of CNFs. More than 100 fibers were analyzed, and average height values were taken for the accuracy of the measurement.

The viscosity of L/CNF suspensions was measured using a constant shear rate vibro viscometer SV-10 (A&D Company, Tokyo, Japan) at 22 °C. Periodic sinusoidal vibrational motion of sensor plates with a frequency of 30 Hz and amplitude <1 mm was utilized for the measurement of viscosity.

The carbon yield of the L/CNF aerogels was determined by dividing the mass of the carbon aerogel obtained after carbonization with the mass of L/CNF aerogels before carbonization. Porosity of the carbon aerogels was measured using eq 1, where ρ_b is the bulk density of CA and ρ_c is the density of amorphous carbon (2.26 g/cm^3).[23]

$$porosity = \left(1 - \frac{\rho_b}{\rho_c}\right) \times 100\% \tag{1}$$

Bulk density was calculated by dividing the mass of CAs with their bulk volume. Bulk volume was obtained by measuring the physical dimensions of CAs. Volume shrinkage during the carbonization process was estimated using eq 2

$$volume\ shrinkage = \frac{V_i - V_f}{V_i} \times 100\% \tag{2}$$

where V_i and V_f are the initial volume before and the final volume after carbonization, respectively.

Thermal properties of individual materials, i.e., lignin and CNFs, were analyzed using a thermogravimetric analyzer (TGA) TA Instruments Q500 (New Castle, DE). TGA was performed in a N_2 atmosphere at a heating rate of 5 K/min, and the temperature profile was similar to that used for the actual carbonization process.

The Brunauer−Emmett−Teller (BET) Micromeritics Gemini VII 2390a (Chemical Instruments AB, Stockholm, Sweden) was used for analyzing the specific surface area (SSA), the average pore size, and the pore volume of the CAs at 77 K. Degassing was done using a Micromeritics FlowPrep060 sample degassing system at 300 °C for 3 h prior to the BET measurement to remove the adsorbed moisture from CAs. The standard t-plot method was used for the analysis of
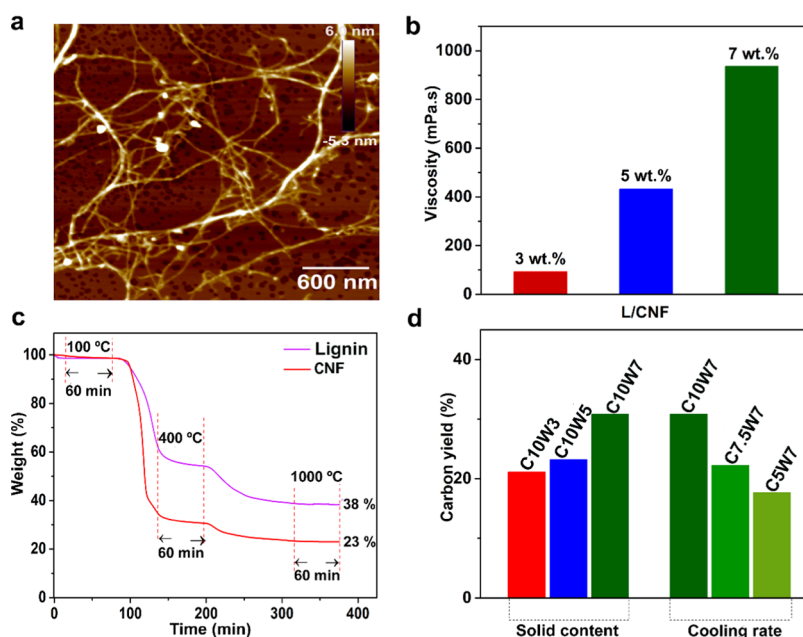
Figure 2. (a) AFM height image for CNFs, (b) viscosity of aqueous L/CNF suspensions measured at around 22 °C, (c) thermal behavior of L and CNFs in similar conditions used for the carbonization process, and (d) carbon yield obtained after carbonization of the L/CNF aerogels at 1000 °C.

micropores, and N_2 adsorbed at a relative pressure $P/P_0 = 0.99$ was utilized for the determination of the total pore volume.

The morphologies of longitudinal and transverse sections of the CAs were investigated using a scanning electron microscopy (SEM) JSM-IT300 JEOL (Tokyo, Japan) under an acceleration voltage of 20 kV. Energy-dispersive X-ray spectroscopy (EDX), using the same SEM instrument equipped with a silicon drift detector (Oxford X-MaxN 50 mm², Oxford Instruments, Abingdon, U.K.), was used for analyzing the elemental composition of CAs. The microstructure of CA was also studied using a high-resolution FE-SEM (Magellan 400 XHR SEM, FEI Company, Hillsboro, OR). To analyze the effect of different cooling rates during ice-templating on the pore structure of CAs, Image J 1.53 e (National Institutes of Health) was used.[24] Three different areas from a single SEM image were chosen, and the fraction of total area occupied by the pores was measured. To increase the accuracy, average values are reported.

X-ray microtomography (XMT) technique was used for the quantitative microstructural analysis of CAs prepared using different cooling rates. Interior tomography scans were carried out using a 3D X-ray microscope (XRM) and a Zeiss Xradia 510 Versa (Carl Zeiss X-ray Microscopy, Pleasanton, CA) using a 20× objective with the field of view 0.5 mm and spatial resolution 0.5 μm (in terms of voxel size). The scanning was carried out with an X-ray tube voltage of 70 kV, a tube power of 6 W, and without any X-ray filters. During a scan, 4501 projection images (radiographs) were acquired, over a sample rotation of 360°, with the exposure time ranging between 3.0 and 3.7 s, which resulted in total scan times in the range of 5.5−6.5 h. The tomographic reconstruction was carried out using filtered back-projection with Zeiss Scout-and-Scan Reconstructor software (version 14.0). The 3D visualization and quantitative analysis of the carbon foam samples were obtained using Dragonfly Pro Software (Object Research Systems, ORS).[25]

Orientation of CNFs in the L/CNF aerogels was studied in the MAX IV synchrotron laboratory (Lund, Sweden) using a NanoMAX beamline, based on the diffractogram of the cellulose crystals. A photon energy of 10 keV was used, which corresponds to a wavelength of 0.123984 nm. The beam size was 250 × 250 nm², and a sample area of 80 × 40 μm² was analyzed in a single scan. The obtained scattering vector q was converted to the scattering angle 2θ using eq 3.

$$q = \frac{4\pi}{\lambda} \sin \theta \tag{3}$$

where λ is the wavelength of the X-ray beam.

Princeton Applied Research VersaSTAT 3 potentiostat/galvanostat (AMETEK Scientific Instruments, Wokingham, U.K.) connected with a three-electrode cell kit (Pine Research Instrumentation, Durham, NC) was used for electrochemical analysis of the CAs. Platinum was used as the counter electrode, and Ag/AgCl was used as the reference electrode. The electrolyte was 1 M sulfuric acid (H_2SO_4). Cyclic voltammetry (CV) measurements were done at different scan rates ranging from 2 to 100 mV s^{-1} in the voltage window of 0−1 V. Specific capacitance from CV measurements was calculated using eq 4

$$C = \frac{1}{mv(V_2 - V_1)} \int_{V_1}^{V_2} I \, dV \tag{4}$$

where C is the specific capacitance in F g^{-1}, m is the mass of active materials loaded as the working electrode in mg, I (A) is the discharge current, v (mV s^{-1}) is the scan rate, and V_1 (V) and V_2 (V) are the lower and upper limits of the voltage window used in the CV test, respectively.

Galvanostatic charge−discharge (GCD) measurements were performed to evaluate the rate capabilities of CAs in the current densities ranging from 0.1 to 1 A g^{-1}. Specific capacitance from GCD was calculated using eq 5
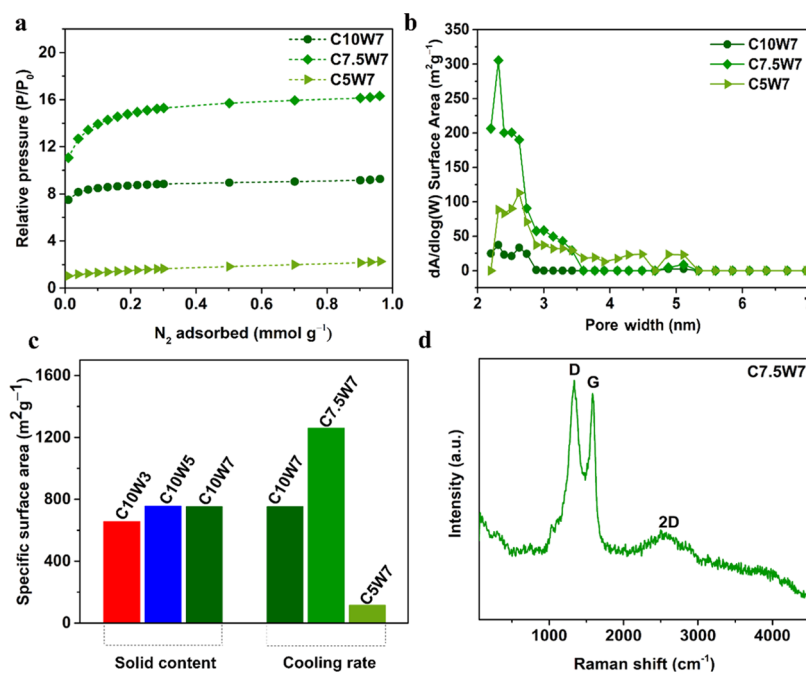
$$C = \frac{I\Delta t}{m\Delta V} \tag{5}$$

where C (F g^{-1}) is the specific capacitance, I (A) is the discharge current, Δt (s) is the discharge time, ΔV (V) is the potential window, and m (mg) is the total mass of the electrode material.

Specific energy density (E) and specific power density (P) derived from galvanostatic tests can be calculated from eqs 6 and 7

$$E = \frac{C\Delta V^2}{2} \tag{6}$$

$$P = \frac{E}{\Delta t} \tag{7}$$

Figure 3. (a) N_2 adsorption isotherms of CAs prepared with different ice-templating cooling rates; (b) pore-size distribution for corresponding CAs; (c) specific surface area of CAs; and (d) Raman spectrum for C7.5W7.

where E (Wh kg^{-1}) is the average energy density, C (F g^{-1}) is the specific capacitance, ΔV (V) is the potential window, P (W kg^{-1}) is the average power density, and Δt (s) is the discharge time.

Cyclic stability studies were performed using the same three-electrode system, and the stability of the CA for 4500 charge–discharge cycles was measured at a current density of 5 A g^{-1}. Electrochemical impedance spectroscopy (EIS) measurements were performed in the frequency range of 10^{-2}–10^5 Hz to determine the resistances of the CAs. Detailed information about the electrochemical measurements performed in this study using the two-electrode system is provided in the Supporting Information.

■ RESULTS AND DISCUSSIONS

Morphology of CNFs used is shown in Figure 2a, whose average width was 4.8 ± 3.4 nm. Viscosities of aqueous suspensions of lignin (L) and CNFs were measured, and the obtained values are graphically shown in Figure 2b and values are shown in Table S1 (given in the Supporting Information). A significant increase in viscosity from 24 to 936 mPa·s was observed when the solid content of L/CNF suspensions was increased from 3 to 7 wt %. The viscosity of the precursor suspensions is important because it affects the nucleation and growth kinetics of ice crystals during the ice-templating process, thus regulating the microstructural features like pore size, pore shape, and wall thickness. Viscosity also plays an important role in 3D macrostructure development and mechanical properties, depending on if the CA is free-standing or collapsible.[18,21,26] In this study, all L/CNF suspensions resulted in free-standing L/CNF aerogels after the lyophilization process.

Thermal degradation of the L and CNFs was studied using TGA, and the results are shown in Figure 2c. L showed a high amount of residue (38.3%) after 1 h at 1000 °C, indicating that it is a good precursor for carbon. CNFs retained 23.1% of the residue at 1000 °C, which indicates that in addition to the function as a rheology modifier in L/CNF suspensions, CNFs would also behave as sacrificial templates by providing porosity during carbonization, a well-established fact supported by

previous studies.[8,11,16] Carbon yield for CAs was varied between 17% (for C5W7) and 30% (for C10W7). It was observed that the solid content in the L/CNF suspensions was linearly related to the final carbon yield, as represented in Figure 2d. The cooling rate during ice-templating is found to have profound effects on the final carbon yield. As the cooling rate was decreased (from 10 to 5 K/min), the carbon yield also decreased (30.8–17.7%). This is likely due to the fact that decreasing the cooling rate resulted in the formation of larger ice crystals during the ice-templating process, which led to the formation of larger and more accessible macropores in the CAs after lyophilization. The latter resulted in the easier release of the volatiles generated during carbonization and consequently decreased the final carbon yield of those CAs.

Bulk density, porosity, and volume shrinkage for all CAs are presented in Table S2 (Supporting Information). Bulk density of CAs varied between 0.017 g cm^{-3} (C10W3) and 0.094 g cm^{-3} (C10W7). It was also observed that with an increase in the solid content (3–7 wt %) the bulk density increased. Bulk porosity was found to be higher than 95% for all CAs, and the volume shrinkage ranged between 64 and 73% for all CAs. Bulk density, porosity, and volume shrinkage for all CAs are presented in Table S2 (in the Supporting Information).

N_2 adsorption isotherms for CAs obtained from the BET analysis are shown in Figures 3a and S1. Corresponding BET surface area values are shown in Figure 3c. From the BET results (Figure 3c), it is evident that the ice-templating cooling rate has the most significant impact on the pore structure and specific surface area of CAs. The highest specific surface area (SSA) of 1260 m^2 g^{-1} was observed for C7.5W7, which was prepared at a cooling rate of 7.5 K/min, while for C10W7 the SSA was 753 m^2 g^{-1} and for C5W7 the SSA reduced drastically to 115 m^2 g^{-1}.

The sharp increase in the adsorption isotherm for C7.5W7 at low relative pressures ($P/P_0 < 0.2$) compared to the other CAs as shown in Figure 3a clearly indicated the presence of a large number of accessible micropores and mesopores.[8,29] This

Table 2. Results from BET Analysis[a]

carbon aerogels	SSA (m^2 g^{-1})	SSA micro (m^2 g^{-1})	SSA meso + macro (m^2 g^{-1})	pore volume (cm^3 g^{-1})	av. pore diameter (nm)	percentage SSA of micropores (%)
C10W3	656.2	502.2	154.0	0.29	1.76	76.5
C10W5	756.1	613.8	142.3	0.32	1.71	81.2
C10W7	753.0	659.9	93.01	0.32	1.70	87.7
C7.5W7	1260	894.6	366.2	0.57	1.79	71.0
C5W7	115.8	26.8	89.1	0.08	2.71	23.1

[a]Specific surface area (SSA), contribution of micropores to SSA, combined SSA by mesopores and macropores, pore volume, average pore diameter, and percentage micropore SSA of the total SSA.
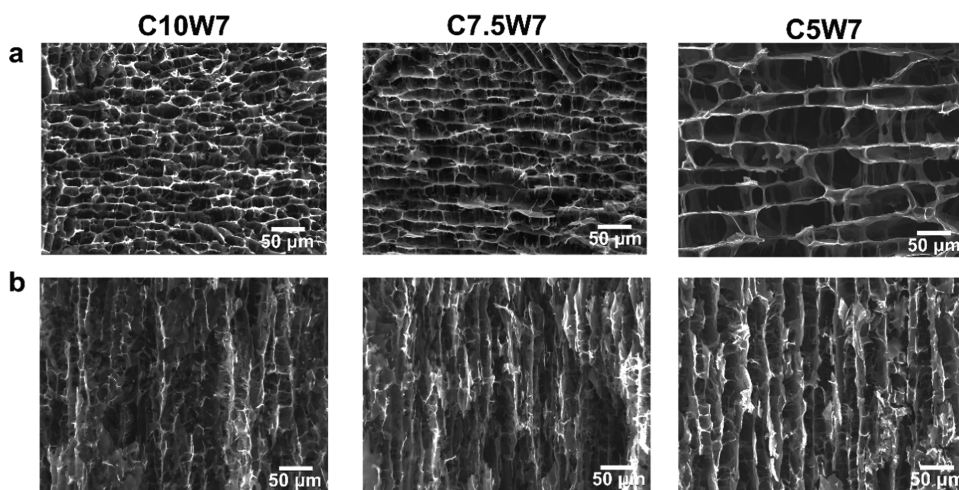
Figure 4. SEM images of L/CNF CAs at different ice-templating cooling rates of 10, 7.5, and 5 K/min. (a) Transverse cross section (perpendicular to the direction of ice crystal growth during ice-templating) and (b) longitudinal section of CAs (parallel to the direction of crystal growth during ice-templating).

is further confirmed by the pore-size distributions shown in Figure 3b, where the C7.5W7 showed a higher contribution of SSA from pore sizes ranging between 2 and 7 nm compared to the other two samples. C7.5W7 also showed the highest pore volume of 0.566 g cm^{-3}, while C5W7 showed the lowest pore volume of 0.079 g cm^{-3}.

All of these results demonstrate that the ice-templating process and especially controlling the cooling rate can be used to tailor the structural evolution of the CAs. Regarding the effect of solid content in the suspensions, the SSA increased from 656 to 756 m^2 g^{-1} when the solid content was increased from 3 to 5 wt %. Further increase of the solid content to 7 wt % had no significant effect on the SSA (753 m^2 g^{-1}). On the other hand, the number of micropores was increased (502 m^2 g^{-1} for C10W3 to 660 m^2 g^{-1} for C10W7), as seen in Table 2. Detailed results from BET analysis are listed in Table 2, and the percentage contributions of micro-, meso-, and macropores are shown graphically in Figure S1b.

The Raman spectrum of C7.5W7 is shown in Figure 3d. Two distinctive characteristic peaks centered at 1340 and 1585 cm^{-1} correspond to D (ring breathing mode of SP^2 carbon atoms in the rings) and G bands (in-plane bond stretching of SP^2 carbon atoms in rings), respectively, and the ratio of intensities I_D/I_G was found to be 1.07, indicating the presence of a graphitic crystalline structure with edge defects and disorders.[30−32] The presence of a broad 2D peak around 2676 cm^{-1} demonstrated the turbostratic carbon structure in the CA.[30,31,33]

The morphologies of the carbon aerogel's transversal and longitudinal sections are shown in Figures 4 and S2.

Micrographs clearly show that all of the CAs possessed an anisotropic microstructure with a honeycomb-like structure in the transverse sections and a parallel-channel-like structure in the longitudinal sections. It was observed from the SEM micrographs (Figure S2 in the Supporting Information) that with the increased solid content from 3 to 7 wt %, the macropore size decreased because of the increased viscosity of L/CNF suspensions, which restrict the lateral ice crystal growth as a result of the generated shear stress. The latter factor induced the creation of more and more nucleation sites on the bottom of the samples, resulting in smaller macropores.[18,20,34] The CAs made under different cooling rates during the ice-templating process showed remarkable differences in their microstructures, as shown in Figure 4 (Figure 4a shows the transverse sections, and Figure 4b shows the longitudinal sections). The macropore size increased as the cooling rate decreased from 10 to 5 K/min. A similar tendency of an increase in pore-size dimensions with a decrease in the cooling rate was reported for ice-templated CNF foams.[19] As discussed in the BET results, the CA exhibited the optimum hierarchical pore structure with the greatest surface area (1260 m^2 g^{-1} with 70% micropores and 30% mesopores and macropores) when the cooling rate was 7.5 K/min. In contrast, a faster cooling rate (10 K/min) developed a larger ratio of micropores (87%), and a slower rate (5 K/min) increased the number of macropores (as shown in Figure 3) to a large extent, resulting in a drastic reduction of SSA. These observations are in accordance with the conclusions obtained from the BET analysis.[18−20]
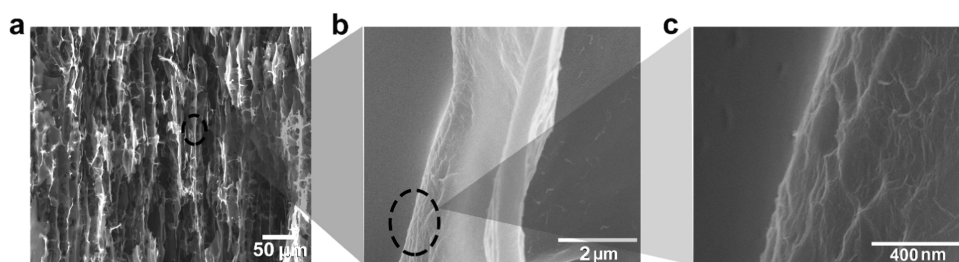
Figure 5. (a) Longitudinal section of C7.5W7. (b) Magnified images of the cell-wall microstructure showing the presence of wrinkled layers in nanodimensions. (c) Enlarged view of the wrinkles circled in Figure 4b.

Cell walls of C7.5W7 (Figure 5a) were observed to have numerous nanosized wrinkles, as shown in Figure 5b,c. To quantify the macropore size variation with the cooling rate, image analysis (Image J software) was used to threshold these microstructures. The resulting porosity and estimated pore sizes (an example of which is shown in Figure S3, Supporting Information) are shown in Table 3. The average macropore

Table 3. Quantitative Measurement of Pore Size and Fraction of Area Covered by Pores in Figure S3 Done Using Image J Software

carbon aerogels	average pore size (μm)	fraction of selected area covered by pores (%)
C10W7	16	16
C7.5W7	23	27
C5W7	66	33

size increased from 16 μm on the fastest cooled ice-templating (at 10 K/min) to 67 μm for the lowest cooling rate (5 K/min), and the corresponding fraction of area covered by pores in the selected area of the image (Figure S3 in the Supporting Information) was increased from 16 to 33%.

Further investigation on the anisotropic structure of CAs was performed using 3D X-ray microtomography (the experimental setup is shown in Figure 6a), and the results confirm the conclusions obtained from SEM analysis. Three-dimensional reconstruction images (Figure 6b) as well as two-dimensional (2D) sectional views of CAs are shown in Figure 6 (transverse and longitudinal directions are shown in Figure 6c,d, respectively). The cell-wall thickness of the CAs with different cooling rates was measured using Dragonfly software. The measurements showed that the cell-wall thickness increased with a decreasing cooling rate from 2.6 $\pm$ 0.3 μm (for 10 K/min) to 2.9 $\pm$ 0.4 μm (for 7.5 K/min), and the highest was for 5 K/min (3.7 $\pm$ 0.4 μm). These results are found to be higher than the wall thickness of previously reported ice-templated CNF foams (0.2−0.4 μm, made from 1 wt % CNF suspension).[19] This could be due to the higher solid content of initial suspensions (7 wt %) and the higher carbon yield as well as the lower volume shrinkage of the CAs caused by the presence of lignin during carbonization.

Figure S4a (in the Supporting Information) shows a representative X-ray diffraction spectrum of the L/CNF precursor aerogels after the integration of the intensities along the radius. Strong cellulose peaks from (200) and (004) planes were observed at 2θ of 22.5 and 34.3°, respectively.[27] The weak peak at approximately 31° can be ascribed to the contribution from sodium (Na).[28] The representative diffractogram for the L/CNF precursor aerogel and the azimuthal integration of the (004) planes are shown in Figure S4b,c. It

can be clearly seen that the relative intensities of the (004) planes did not change noticeably, indicating that the CNFs were randomly oriented in the aerogel.

Elemental analysis of the CAs indicates (shown the Table S3 in the Supporting Information) that the carbon content varied between 88 and 95 atomic percentage (at %), the oxygen content was between 3 and 11 at %, and minor amounts of Na (<2 at %) and S (<1 at %) were present, which could be due to the high purity of lignin derived from the isolation process.[35]

Figure 7 shows the electrochemical properties of prepared CAs measured using a three-electrode cell with 1 M H_2SO_4 as the electrolyte. From CV and GCD measurements, the highest electrochemical performance was observed for C7.5W7, with a specific capacitance of 410 F g^{-1} at 2 mV s^{-1} and 303.5 F g^{-1} at 0.1 A g^{-1}. As shown in Figure 7a, CVs were near-rectangular-shaped at lower scan rates, and Figure 7b shows the deviation to a quasi-rectangular shape toward the higher scan rates. Figure 7c,d shows the CV and GCD curves for C7.5W7 at different scan rates and current densities. Figure 7a,b clearly illustrates that the decrease of the cooling rate from 10 to 7.5 K/min remarkably improved the electrochemical performance of the CAs because of the 66% increase in their SSA (from 753 to 1260 m^{2}g^{-1}), as mentioned in BET results. It is also important to note that at 7.5 K/min the carbon structure contained more mesopores, approximately 30%, compared to nearly only 12% of mesopores at 10 K/min, which is likely beneficial for achieving high electrochemical performance as mentioned earlier. Further reduction in the cooling rate to 5 K/min led to a very low SSA (115 m^{2}g^{-1}) and larger macropores as observed in morphology analysis (shown in Figures 4 and 6). The resulting macropores could not act as charge reservoirs during the charging and discharging processes, leading to poor electrochemical performance (19.5 F g^{-1} at 2 mV s^{-1} and 7.4 F g^{-1} at 0.1 A g^{-1}). Thus, a cooling rate of 7.5 K/min was found to be an optimum value to have both a good hierarchical porous structure and superb electrochemical performances. While comparing the electro-chemical performances of CAs prepared using suspensions of different solid contents, C10W7 showed a higher specific capacitance (190 F g^{-1} at 2 mV s^{-1}) than C10W5 (136 F g^{-1} at 2 mV s^{-1}) and C10W3 (110 F g^{-1} at 2 mV s^{-1}). Even though the BET surface areas for C10W7 and C10W5 were observed to be similar, as shown in Table 2, the higher percentage of accessible micropores could be the reason for the high SC for C10W7. Figure 7e,f represents the capacitance values obtained for CAs from CV (values are provided in Table S4 in the Supporting Information) and GCD measurements (values are given in Table S5 in the Supporting Information), respectively, at different scan rates and current densities.
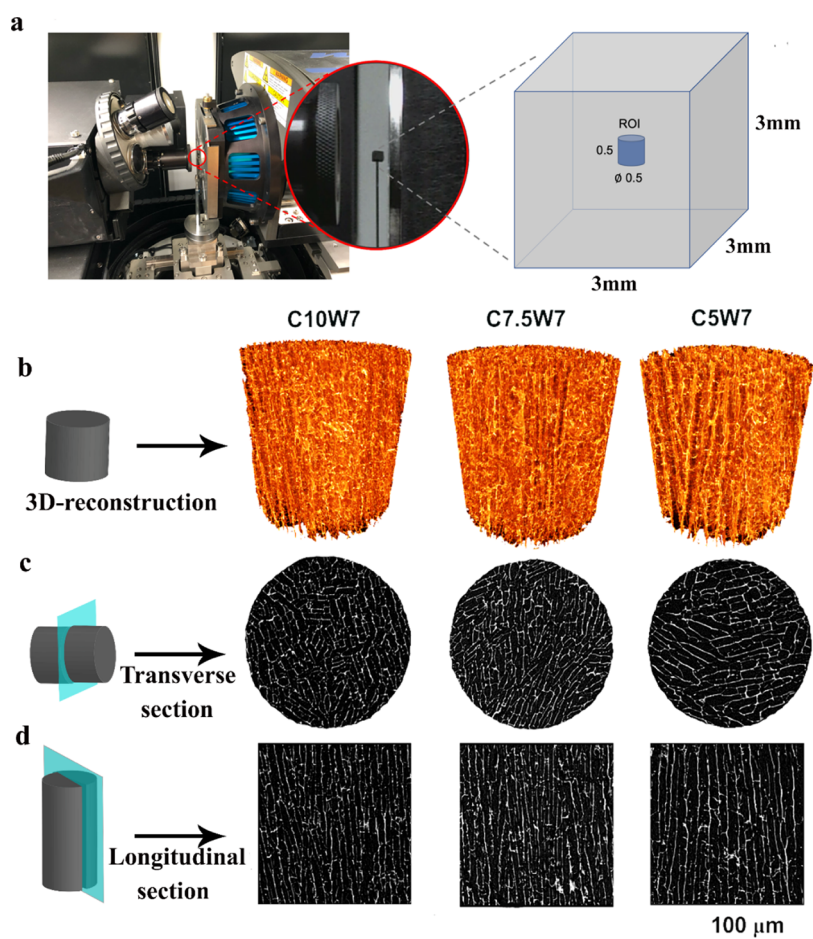
Figure 6. Three-dimensional X-ray microtomography results for CAs prepared using different ice-templating cooling rates (10, 7.5, 5 K/min). (a) Experimental setup of the XMT-scanning showing the Zeiss Xradia 510 Versa system, a close-up of the carbon foam sample, and the position and dimension of the reconstructed ROI within the sample; (b) 3D reconstruction of CAs (c) and (d) 2D slices of the CAs in the transverse and longitudinal sections, respectively.

The best CA (C7.5W7) was also further investigated as a free-standing electrode; two-electrode measurements were performed to demonstrate the electrochemical performance of the electrode when it was mounted as a practical supercapacitor (SC). A schematic illustration of the SC assembly is shown in Figure S8 in the Supporting Information. Figure 8a shows the physical dimensions of the electrode material (approximately 6 mm wide and 11 mm long, and mass 5.3 mg). The electrode was completely submerged in 1 M H_2SO_4 without deformation, indicating good wettability of the CA in the electrolyte. As observed from Figure 8b,c, CV curves were nearly rectangular even at higher scan rates and GCD curves were also symmetrical, indicating the good capacitive behavior of this CA (C7.5W7). A high specific capacitance of 240 F g^{-1} was obtained at 0.1 A g^{-1} from the GCD analysis (as shown in Figure 8d), which is 150 and 190% higher than the capacitance values obtained from similar CAs reported by Thomas et al.[8] and Geng et al.[11] at the same current density. The Ragone plot for the SC is shown in Figure 8e, and the highest energy density of 8.3 Wh kg^{-1} was observed for a power density of 50 W kg^{-1}. Figure 8f shows the comparison of specific capacitances reported for different carbon SC electrodes prepared from lignin as well as other sources, and Table S6 shows the list of different parameters used for analysis of their electrochemical characteristics. Even though the specific capacitance values are depending on different

parameters used for the electrochemical measurements, which makes the direct comparison difficult, C7.5W7 showed high SSA and good specific capacitance compared to different carbon electrodes reported in the literature.[1,4,5,8,11,13]

Electrochemical impedance spectroscopy (EIS) was conducted for the in-depth analysis of the capacitive behavior of the C7.5W7 electrode. Proper selection of the separator material and the low bulk solution resistance of the electrolyte led to negligible equivalent series resistance of nearly zero as shown in the Nyquist plot (Figure 9a). Meanwhile, the relatively low charge-transfer resistance (R_{CT}) of approximately 10 Ω indicates both the good contact of the electrodes with current collectors and the well-interconnected porous structure in the C7.5W7 electrode resulting in low contact resistance and low ionic resistance, respectively.[36,37] Figure 9b shows the variation of absolute impedance (|Z|) with frequency, and the Bode plot in Figure 9c represents the capacitor response frequency, f_0, at a phase angle of 45°. For the current supercapacitor assembly, the response frequency was found to be 0.12 Hz, indicating that the SC would exhibit pure capacitive behavior below the "knee frequency", 0.12 Hz. The phase angle of the SC was found to be around 71° at the frequency of 0.01 Hz (Figure 9c), which is comparable to ideal supercapacitors having a phase angle of 90°.[38]

Figure 9d,e shows the variation of real and imaginary parts of capacitances, respectively, against frequency. The imaginary
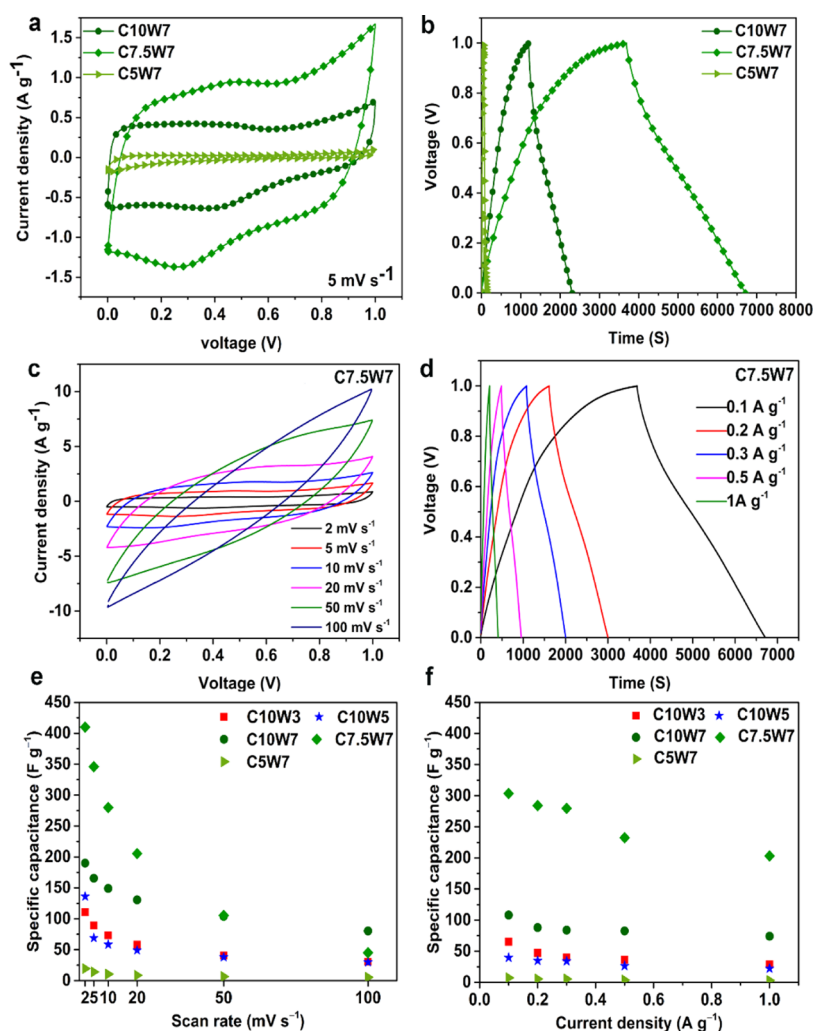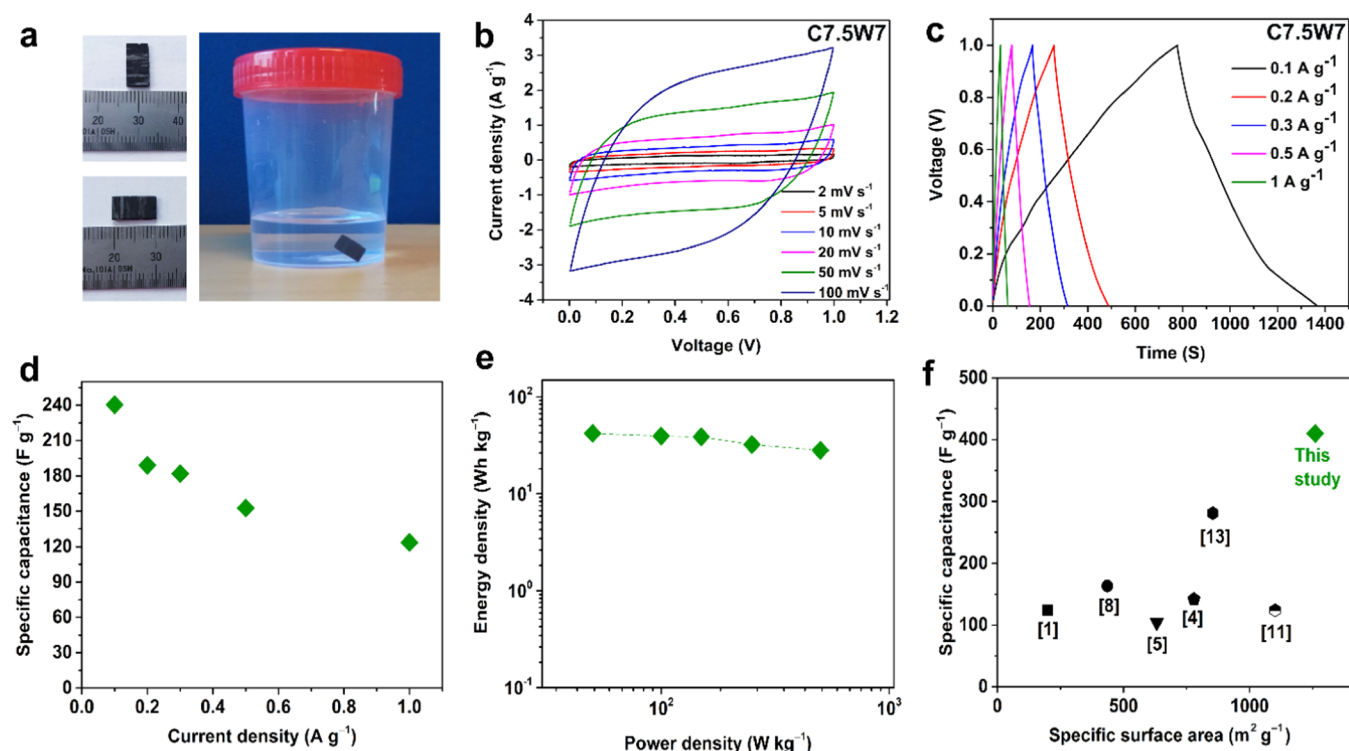
Figure 7. Electrochemical behavior of CAs obtained from the three-electrode method. (a, b) Comparison of CVs (scan rate 5 mV s^{-1}) and GCDs (current density 0.1 A g^{-1}) obtained for CAs prepared using different ice-templating cooling rates. (c, d) CVs and GCDs of best-performing C7.5W7 at different scan rates and current densities, respectively. (e, f) Specific capacitances (F g^{-1}) of CAs at different scan rates and current densities obtained from CV and GCD analyses.

component of capacitance shows a peak, and the intercept to the maximum gives the response frequency from which the relaxation time constant for the SC can be calculated. The relaxation time constant τ_0 ($\tau_0 = 1/\omega_0$) was found to be 1.3 s, indicating the fast response of SC to deliver the stored charges during discharging. The relaxation time constant obtained in this study is superior compared to the biomass-based activated carbon SC electrodes[39,40] and is comparable to chemically activated graphene-based SC electrodes.[38,41] The cyclic stability of C7.5W7 electrodes has been analyzed using a three-electrode system at the current density of 3 A g^{-1}, and the obtained charge−discharge cycles are represented in Figure 9f. After 4500 charge−discharge cycles, C7.5W7 electrodes showed an excellent cyclic stability of 93.8% and good structural integrity even after cyclic stability analysis, as shown in Figure S6. The undisturbed microstructure in Figure S6 clearly indicates that the CAs possess good mechanical strength and handleability to be able to use as stable SC electrodes like the already-reported lignin-based CAs by Thomas et al.[8] All of these results show the suitability of these materials as potential SC electrodes with a long lifespan.

■ CONCLUSIONS

This study aimed to better understand the ice-templating process mechanism including processing parameters such as the cooling rate and solid content of lignin and the cellulose nanofiber suspension with an emphasis on the influence of the hierarchical porous structure and consequently electrochemical characteristics of the carbon aerogels. The cooling rate was shown to be the most influential factor in designing the structure of CAs to achieve outstanding electrochemical performance, while the solid content showed little influence. The CA prepared using 7.5 K/min as the cooling rate from the suspension with 7 wt % solid content (C7.5W7) possessed the hierarchical porous structure containing numerous pores in nanometer dimensions along with nanosized surface wrinkles, which resulted in the highest surface area of 1260 m^2 g^{-1} and demonstrated an excellent specific capacitance of 410 F g^{-1} at 2 mV s^{-1}. The practical symmetric supercapacitor assembled using C7.5W7 CAs as electrodes also showed a remarkable capacitance of 240 F g^{-1} at 0.1 A g^{-1}. The current SC exhibited a good energy density of 8.3 Wh kg^{-1} at a power density of 50 W kg^{-1} and 4.3 Wh kg^{-1} at a power density of 500 W kg^{-1}, and the cyclic stability of the electrodes after 4500

Figure 8. Electrochemical behavior of the C7.5W7 analyzed using the two-electrode method. (a) Images showing the actual dimensions of the electrode used for the study and its wettability in 1 M H2SO4. (b, c) CVs and GCDs for the CA materials at different scan rates and current densities. (d) Specific capacitance obtained for the CA electrode at different current densities. (e) Ragone plot showing the energy density of CA at different power densities. (f) Comparison of the specific capacitance vs SSA for C7.5W7 with the already-reported carbon-based SC electrodes.
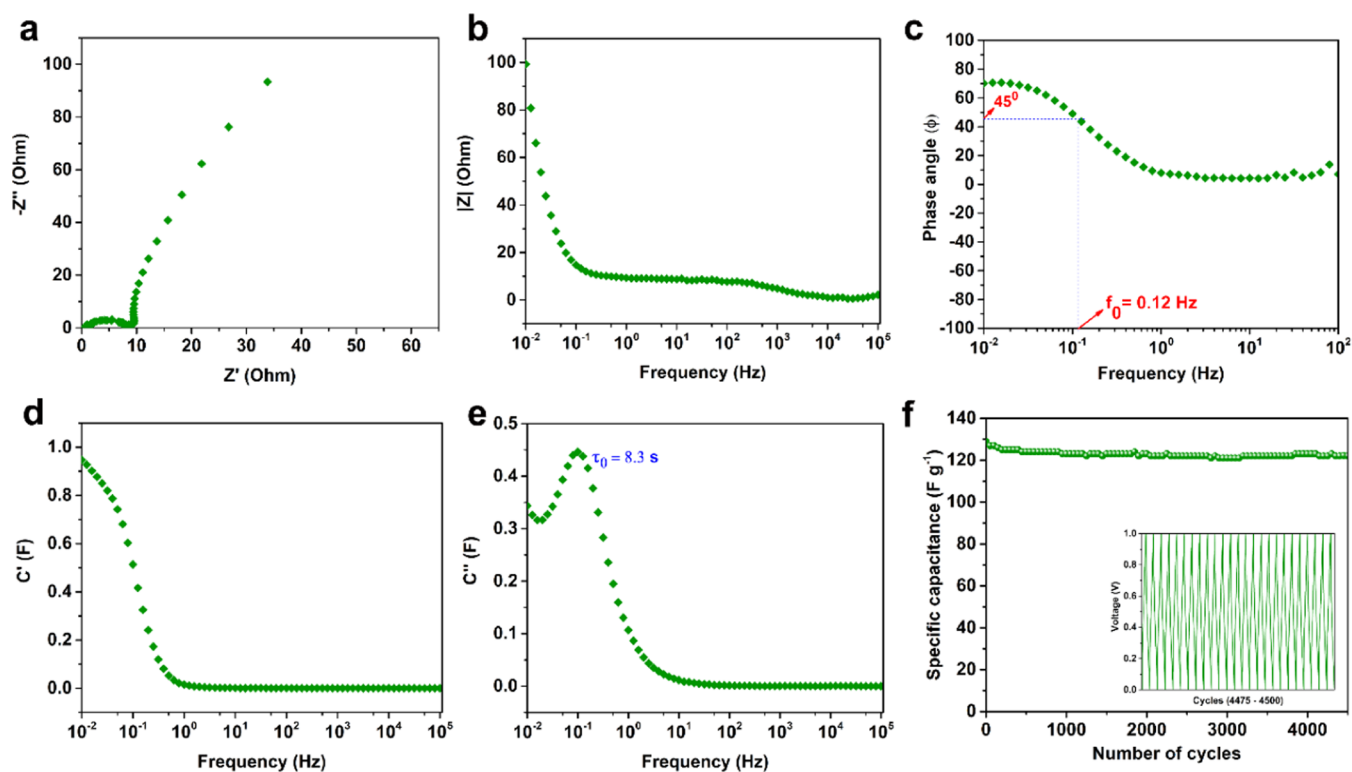
Figure 9. Electrochemical impedance spectroscopy (EIS) results obtained from the two-electrode analysis for C7.5W7. (a) Nyquist plot of CA in the frequency range between 10−2 and 105 Hz. (b) Variation of absolute impedance |Z| (Ohm) vs frequency (Hz). (c) Bode plot showing the characteristic frequency (f_0). Evolution of real (d) and imaginary (e) capacitance with respect to the frequency. (f) Cyclic stability of the electrode up to 4500 charge−discharge cycles measured using the three-electrode system, and the inset showing the charge−discharge cycles during GCD analysis from 4475 to 4500 cycles.

charge—discharge cycles was 94%. Moreover, the prepared CA electrodes are free-standing and binder-free, and no special activation steps were needed, indicating their versatile potential to be used in SCs for future energy storage applications. In addition to energy storage, the idea of controlling the ice-templating parameters to tune the structure can be beneficial for developing hierarchically porous materials for other applications like EMI shielding, CO_2 adsorption, carbon aerogel composites, insulation materials, etc.

■ ASSOCIATED CONTENT

Ⓢ Supporting Information

The Supporting Information is available free of charge at https://pubs.acs.org/doi/10.1021/acsanm.2c01033.

Viscosity, conductivity, and pH of L/CNF suspensions (Table S1); physical properties of CAs, bulk density, bulk porosity, and volume shrinkage of CAs after carbonization (Table S2); results obtained from energy-dispersive X-ray spectroscopy (EDX). elemental composition of carbon aerogels (Table S3); specific capacitance values at different scan rates from cyclic voltammetry (CV) measurement (Table S4); specific capacitance values at different scan rates from galvanostatic charge—discharge measurement (Table S5); comparison of SCs made from different carbon materials, analysis conditions, and their specific capacitances (Table S6); N_2 adsorption isotherms of CAs prepared with different suspensions having different solid contents during ice-templating. N_2 adsorption isotherms of CAs and graphical representation of percentage of micro-, meso-, and macropores in the CA (Figure S1); effect of solid content on the microstructure of L/CNF based carbon aerogels (Figure S2); image analysis performed on the cross-sectional micrographs of C7.5W7 (Figure S3); results from the orientation study for L/CNF precursor aerogels (Figure S4); cyclic voltammetry results from the three-electrode system of measurement for CAs at different scanning rates (Figure S5); microstructure of C7.5W7 after the cyclic stability analysis (Figure S6) and the supercapacitor assembly (Figure S6) (PDF)

(MP4)

(MP4)

(MP4)

■ AUTHOR INFORMATION

Corresponding Author

Kristiina Oksman − *Division of Materials Science, Department of Engineering Sciences and Mathematics, Luleå University of Technology, SE-971 87 Luleå, Sweden; Department of Mechanical & Industrial Engineering (MIE), University of Toronto, Toronto, Ontario M5S 3G8, Canada; Wallenberg Wood Science Center (WWSC), Luleå University of Technology, SE-97187 Luleå, Sweden;* ⓘ orcid.org/0000-0003-4762-2854; Phone: +46 70 358 5371; Email: kristiina.oksman@ltu.se

Authors

Bony Thomas − *Division of Materials Science, Department of Engineering Sciences and Mathematics, Luleå University of Technology, SE-971 87 Luleå, Sweden*

Shiyu Geng − *Division of Materials Science, Department of Engineering Sciences and Mathematics, Luleå University of Technology, SE-971 87 Luleå, Sweden;* ⓘ orcid.org/0000-0003-1776-2725

Jiayuan Wei − *Division of Materials Science, Department of Engineering Sciences and Mathematics, Luleå University of Technology, SE-971 87 Luleå, Sweden;* ⓘ orcid.org/0000-0002-1484-7224

Henrik Lycksam − *Division of Fluid and Experimental Mechanics, Department of Engineering Sciences and Mathematics, Luleå University of Technology, SE-971 87 Luleå, Sweden*

Mohini Sain − *Division of Materials Science, Department of Engineering Sciences and Mathematics, Luleå University of Technology, SE-971 87 Luleå, Sweden; Department of Mechanical & Industrial Engineering (MIE), University of Toronto, Toronto, Ontario M5S 3G8, Canada;* ⓘ orcid.org/0000-0003-0808-271X

Complete contact information is available at:
https://pubs.acs.org/10.1021/acsanm.2c01033

Author Contributions

B.T.: Conceptualization, data curation, formal analysis, investigation, methodology, validation, visualization, writing—original draft, writing—review & editing. S.G.: Conceptualization, formal analysis, investigation, supervision, writing—review & editing. J.W.: Investigation, writing—review & editing. H.L.: Investigation, writing—review & editing. M.S.: Resources, supervision, writing—review & editing. K.O.: Conceptualization, funding acquisition, project administration, resources, supervision, writing—review & editing.

Notes

The authors declare no competing financial interest.

■ ACKNOWLEDGMENTS

■ REFERENCES

(1) Xu, X.; Zhou, J.; Nagaraju, D. H.; Jiang, L.; Marinov, V. R.; Lubineau, G.; Alshareef, H. N.; Oh, M. Flexible, Highly Graphitized Carbon Aerogels Based on Bacterial Cellulose/Lignin: Catalyst-Free Synthesis and Its Application in Energy Storage Devices. *Adv. Funct. Mater.* **2015**, *25*, 3193−3202.

(2) Zhang, Y.; Zhao, C.; Ong, W. K.; Lu, X. Ultrafast-Freezing-Assisted Mild Preparation of Biomass-Derived, Hierarchically Porous, Activated Carbon Aerogels for High-Performance Supercapacitors. *ACS Sustainable Chem. Eng.* **2019**, *7*, 403−411.

(3) Sam, D. K.; Sam, E. K.; Durairaj, A.; Lv, X.; Zhou, Z.; Liu, J. Synthesis of Biomass-Based Carbon Aerogels in Energy and Sustainability. *Carbohydr. Res.* **2020**, *491*, No. 107986.

(4) Xu, J.; Zhou, X.; Chen, M.; Shi, S.; Cao, Y. Preparing Hierarchical Porous Carbon Aerogels Based on Enzymatic Hydrolysis Lignin through Ambient Drying for Supercapacitor Electrodes. *Microporous Mesoporous Mater.* **2018**, *265*, 258−265.

(5) Li, W.; Reichenauer, G.; Fricke, J. Carbon Aerogels Derived from Cresol-Resorcinol-Formaldehyde for Supercapacitors. *Carbon* **2002**, *40*, 2955−2959.

(6) Liu, H. J.; Cui, W. J.; Jin, L. H.; Wang, C. X.; Xia, Y. Y. Preparation of Three-Dimensional Ordered Mesoporous Carbon Sphere Arrays by a Two-Step Templating Route and Their Application for Supercapacitors. *J. Mater. Chem.* **2009**, *19*, 3661−3667.

(7) Liu, F.; Wang, Z.; Zhang, H.; Jin, L.; Chu, X.; Gu, B.; Huang, H.; Yang, W. Nitrogen, Oxygen and Sulfur Co-Doped Hierarchical Porous Carbons toward High-Performance Supercapacitors by Direct Pyrolysis of Kraft Lignin. *Carbon* **2019**, *149*, 105−116.

(8) Thomas, B.; Geng, S.; Sain, M.; Oksman, K. Hetero-Porous, High-Surface Area Green Carbon Aerogels for the next-Generation Energy Storage Applications. *Nanomaterials* **2021**, *11*, No. 653.

(9) Abdelaziz, O. Y.; Hulteberg, C. P. Physicochemical Characterisation of Technical Lignins for Their Potential Valorisation. *Waste Biomass Valorization* **2017**, *8*, 859−869.

(10) Bajwa, D. S.; Pourhashem, G.; Ullah, A. H.; Bajwa, S. G. A Concise Review of Current Lignin Production, Applications, Products and Their Environment Impact. *Ind. Crops Prod.* **2019**, *139*, No. 111526.

(11) Geng, S.; Wei, J.; Jonasson, S.; Hedlund, J.; Oksman, K. Multifunctional Carbon Aerogels with Hierarchical Anisotropic Structure Derived from Lignin and Cellulose Nanofibers for CO2 Capture and Energy Storage. *ACS Appl. Mater. Interfaces* **2020**, *12*, 7432−7441.

(12) Zhao, B.; Borghei, M.; Zou, T.; Wang, L.; Johansson, L.-S.; Majoinen, J.; Sipponen, M. H.; Österberg, M.; Mattos, B. D.; Rojas, O. J. Lignin-Based Porous Supraparticles for Carbon Capture. *ACS Nano* **2021**, *15*, 6774−6786.

(13) Liu, W.; Yao, Y.; Fu, O.; Jiang, S.; Fang, Y.; Wei, Y.; Lu, X. Lignin-Derived Carbon Nanosheets for High-Capacitance Supercapacitors. *RSC Adv.* **2017**, *7*, 48537−48543.

(14) Zeng, Z.; Zhang, Y.; Ma, X. Y. D.; Shahabadi, S. I. S.; Che, B.; Wang, P.; Lu, X. Biomass-Based Honeycomb-like Architectures for Preparation of Robust Carbon Foams with High Electromagnetic Interference Shielding Performance. *Carbon* **2018**, *140*, 227−236.

(15) Zeng, Z.; Wang, C.; Zhang, Y.; Wang, P.; Seyed Shahabadi, S. I.; Pei, Y.; Chen, M.; Lu, X. Ultralight and Highly Elastic Graphene/Lignin-Derived Carbon Nanocomposite Aerogels with Ultrahigh Electromagnetic Interference Shielding Performance. *ACS Appl. Mater. Interfaces* **2018**, *10*, 8205−8213.

(16) Geng, S.; Maennlein, A.; Yu, L.; Hedlund, J.; Oksman, K. Monolithic Carbon Aerogels from Bioresources and Their Application for CO$_2$ Adsorption. *Microporous Mesoporous Mater.* **2021**, *323*, No. 111236.

(17) Chen, Y.; Li, S.; Li, X.; Mei, C.; Zheng, J.; E, S.; Duan, G.; Liu, K.; Jiang, S. Liquid Transport and Real-Time Dye Purification via Lotus Petiole-Inspired Long-Range-Ordered Anisotropic Cellulose Nanofibril Aerogels. *ACS Nano* **2021**, *15*, 20666−20677.

(18) Deville, S. Ice-Templating, Freeze Casting: Beyond Materials Processing. *J. Mater. Res.* **2013**, *28*, 2202−2219.

(19) Wicklein, B.; Kocjan, A.; Salazar-Alvarez, G.; Carosio, F.; Camino, G.; Antonietti, M.; Bergström, L. Thermally Insulating and Fire-Retardant Lightweight Anisotropic Foams Based on Nanocellulose and Graphene Oxide. *Nat. Nanotechnol.* **2015**, *10*, 277−283.

(20) Deville, S.; Saiz, E.; Tomsia, A. P. Ice-Templated Porous Alumina Structures. *Acta Mater.* **2007**, *55*, 1965−1974.

(21) Gutiérrez, M. C.; Ferrer, M. L.; del Monte, F. Ice-Templated Materials: Sophisticated Structures Exhibiting Enhanced Functionalities Obtained after Unidirectional Freezing and Ice-Segregation-Induced Self-Assembly. *Chem. Mater.* **2008**, *20*, 634−648.

(22) Berglund, L.; Noël, M.; Aitomäki, Y.; Öman, T.; Oksman, K. Production Potential of Cellulose Nanofibers from Industrial Residues: Efficiency and Nanofiber Characteristics. *Ind. Crops Prod.* **2016**, *92*, 84−92.

(23) Bhattarai, B.; Pandey, A.; Drabold, D. A. Evolution of Amorphous Carbon across Densities: An Inferential Study. *Carbon* **2018**, *131*, 168−174.

(24) Schneider, C. A.; Rasband, W. S.; Eliceiri, K. W. NIH Image to ImageJ: 25 Years of Image Analysis. *Nat. Methods* **2012**, *9*, 671−675.

(25) Berglund, L.; Nissilä, T.; Sivaraman, D.; Komulainen, S.; Telkki, V.-V.; Oksman, K. Seaweed-Derived Alginate−Cellulose Nanofiber Aerogel for Insulation Applications. *ACS Appl. Mater. Interfaces* **2021**, *13*, 34899−34909.

(26) Yang, J.; Yang, W.; Chen, W.; Tao, X. An Elegant Coupling: Freeze-Casting and Versatile Polymer Composites. *Prog. Polym. Sci.* **2020**, *109*, No. 101289.

(27) Nissilä, T.; Wei, J.; Geng, S.; Teleman, A.; Oksman, K. Ice-Templated Cellulose Nanofiber Filaments as a Reinforcement Material in Epoxy Composites. *Nanomaterials* **2021**, *11*, 490.

(28) Su, L.; Fang, G. Characterization of Cross-Linked Alkaline Lignin/Poly (Vinyl Alcohol) Film with a Formaldehyde Cross-Linker. *BioResources* **2014**, *9*, 4477−4488.

(29) Kleszyk, P.; Ratajczak, P.; Skowron, P.; Jagiello, J.; Abbas, Q.; Frąckowiak, E.; Béguin, F. Carbons with Narrow Pore Size Distribution Prepared by Simultaneous Carbonization and Self-Activation of Tobacco Stems and Their Application to Supercapacitors. *Carbon* **2015**, *81*, 148−157.

(30) Li, T.; Zhi, D.; Chen, Y.; Li, B.; Zhou, Z.; Meng, F. Multiaxial Electrospun Generation of Hollow Graphene Aerogel Spheres for Broadband High-Performance Microwave Absorption. *Nano Res.* **2020**, *13*, 477−484.

(31) Nan, H.; Luo, F.; Jia, H.; Pan, H.; Huang, Z.; Deng, H.; Qing, Y.; Wang, C.; Chen, Q. The Effect of Temperature on Structure and Permittivity of Carbon Microspheres as Efficient Absorbent Prepared by Facile and Large-Scale Method. *Carbon* **2021**, *185*, 650−659.

(32) Wang, H.; Xu, Z.; Kohandehghan, A.; Li, Z.; Cui, K.; Tan, X.; Stephenson, T. J.; King'Ondu, C. K.; Holt, C. M. B.; Olsen, B. C.; Tak, J. K.; Harfield, D.; Anyia, A. O.; Mitlin, D. Interconnected Carbon Nanosheets Derived from Hemp for Ultrafast Supercapacitors with High Energy. *ACS Nano* **2013**, *7*, 5131−5141.

(33) Jin, J.; Ding, J.; Klett, A.; Thies, M. C.; Ogale, A. A. Carbon Fibers Derived from Fractionated-Solvated Lignin Precursors for Enhanced Mechanical Performance. *ACS Sustainable Chem. Eng.* **2018**, *6*, 14135−14142.

(34) Martoïa, F.; Dumont, P. J. J.; Orgéas, L.; Belgacem, M. N.; Putaux, J. L. Micro-Mechanics of Electrostatically Stabilized Suspensions of Cellulose Nanofibrils under Steady State Shear Flow. *Soft Matter* **2016**, *12*, 1721−1735.

(35) Zhu, W.; Westman, G.; Theliander, H. Investigation and Characterization of Lignin Precipitation in the LignoBoost Process. *J. Wood Chem. Technol.* **2014**, *34*, 77−97.

(36) Mei, B. A.; Lau, J.; Lin, T.; Tolbert, S. H.; Dunn, B. S.; Pilon, L. Physical Interpretations of Electrochemical Impedance Spectroscopy of Redox Active Electrodes for Electrical Energy Storage. *J. Phys. Chem. C* **2018**, *122*, 24499−24511.

(37) Subramanian, V.; Zhu, H.; Wei, B. Synthesis and Electrochemical Characterizations of Amorphous Manganese Oxide and Single Walled Carbon Nanotube Composites as Supercapacitor Electrode Materials. *Electrochem. Commun.* **2006**, *8*, 827−832.

(38) Kim, T.; Jung, G.; Yoo, S.; Suh, K. S.; Ruoff, R. S. Activated Graphene-Based Carbons as Supercapacitor Electrodes with Macro- and Mesopores. *ACS Nano* **2013**, *7*, 6899−6905.

(39) Wang, K.; Zhao, N.; Lei, S.; Yan, R.; Tian, X.; Wang, J.; Song, Y.; Xu, D.; Guo, Q.; Liu, L. Promising Biomass-Based Activated Carbons Derived from Willow Catkins for High Performance Supercapacitors. *Electrochim. Acta* **2015**, *166*, 1−11.

(40) Cheng, P.; Gao, S.; Zang, P.; Yang, X.; Bai, Y.; Xu, H.; Liu, Z.; Lei, Z. Hierarchically Porous Carbon by Activation of Shiitake Mushroom for Capacitive Energy Storage. *Carbon* **2015**, *93*, 315−324.

(41) Sun, X.; Cheng, P.; Wang, H.; Xu, H.; Dang, L.; Liu, Z.; Lei, Z. Activation of Graphene Aerogel with Phosphoric Acid for Enhanced Electrocapacitive Performance. *Carbon* **2015**, *92*, 1−10.